Multidimensional Clutter Filtering of Aperture Domain Data for Improved Blood Flow Sensitivity

Kathryn A. Ozgun, *Graduate Student Member, IEEE*, and Brett C. Byram, *Member, IEEE*

***Abstract*— Singular value decomposition (SVD) is a valuable factorization technique used in clutter rejection filtering for power Doppler imaging. Conventionally, SVD is applied to a Casorati matrix of radio frequency data, which enables filtering based on spatial or temporal characteristics. In this article, we propose a clutter filtering method that uses a higher order SVD (HOSVD) applied to a tensor of aperture data, e.g., delayed channel data. We discuss temporal, spatial, and aperture domain features that can be leveraged in filtering and demonstrate that this multidimensional approach improves sensitivity toward blood flow. Further, we show that HOSVD remains more robust to short ensemble lengths than conventional SVD filtering. Validation of this technique is shown using Field II simulations and *in vivo* data.**

***Index Terms*— Blood flow, clutter rejection, higher order SVD (HOSVD), power Doppler (PD), singular value decomposition (SVD).**

I. Introduction

POWER Doppler (PD) imaging is a preferred ultrasonic technique for visualization of low-velocity blood flow. When coupled with plane wave synthetic focusing (PWSF), Doppler data can be accumulated at high frame rates with improved sensitivity toward microvasculature [1], [2]. This has enabled visualization of low-velocity blood flow without contrast enhancement, which is clinically valuable for functional and therapeutic assessment [2], [3].

However, the sensitivity of PD imaging is inherently tied to the signal-to-clutter ratio (SCR) and the filter rejection band [2]. These constraints particularly impede microvasculature imaging, as low-velocity blood echoes are often close to the noise floor [4], [5] and can exhibit similar slow-time characteristics to tissue [4], [5]. For noncontrast PD, these challenges have been primarily addressed through novel beamforming [6]–[9], clutter rejection [10]–[16], and postprocessing strategies [5], [17].

Clutter rejection filtering is used to suppress undesirable noise and "clutter" signals, which arise from reverberation, OFF-axis scattering, and nonstationary tissue echoes [16], [18]. Historically, clutter rejection algorithms have used infinite impulse response, finite impulse response, and regression filters, which have been extensively studied and optimized [19]–[22]. These filters are effective when the blood and clutter signals reside in orthogonal Fourier or polynomial basis vectors; however, this assumption can be violated in imaging conditions with patient and sonographer motion as well as in conditions with strong electronic white noise [16], [18]. Frequently, clutter rejection filters are coupled with motion correction techniques to reduce the mean frequency and bandwidth of the clutter signal [20], [23].

More recently, singular value decomposition (SVD) filters have emerged as a robust alternative to conventional filters. The motivation for using SVD filters is twofold. First, SVD filtering is inherently adaptive, as the SVD basis set is defined by the covariance characteristics of the data. In addition, SVD filters can operate on 1-D (temporal) or 2-D (spatial and temporal) data, which expands the feature space for signal classification. As a result, SVD filtering can achieve superior performance over conventional methods [11], [14]–[16].

However, SVD filter utility suffers when blood, clutter, and noise are not distributed over orthogonal bases. Complex tissue motions and factorization rank limitations can cause signal overlap, which imposes a trade-off between clutter rejection and preservation of the blood signal [5], [12]. Accordingly, SVD filtering improves with longer ensemble sizes [14], [15], but this is not feasible on clinical scanners which rely on short ensemble lengths (typically <50 frames) to achieve reasonable real-time Doppler frame rates [24], [25].

Higher order SVD (HOSVD) filtering has been proposed to improve the SCR while preserving sensitivity toward microvasculature. The application of HOSVD was first proposed by Kim *et al.* [26], [27] who demonstrated efficacy in filtering a 3-D tensor of multirate radio frequency data. This method has been termed multirate because it employs two temporal dimensions, namely, the pulse dimension, which is sampled on the slow time interval at the pulse repetition

Manuscript received March 5, 2021; accepted April 11, 2021. Date of publication April 14, 2021; date of current version July 26, 2021. This work was supported in part by the National Institute of Biomedical Imaging and Bioengineering under Grant T32-EB021937, and in part by the National Science Foundation Award under Grant IIS-1750994. *(Corresponding author: Kathryn A. Ozgun.)*

The authors are with the Department of Biomedical Engineering, Vanderbilt University, Nashville, TN 37235 USA (e-mail: kathryn.a.ozgun@vanderbilt.edu).

Digital Object Identifier 10.1109/TUFFC.2021.3073292

frequency (PRF), and the Doppler frame dimension, which constitutes a set of pulses. Expanding the dimensionality of the data expands the feature space, which enables better separability of the blood signal.

To date, research on clutter rejection filtering has been limited to temporal and spatial extents. However, advancements in PD beamforming have primarily focused on leveraging features of delayed channel data and subaperture data [10]–[16]. With the exception of limited research [28], [29], these features have remained broadly unstudied for clutter filtering.

In this article, we present a novel filtering methodology that uses a HOSVD applied to a 3-D tensor of aperture data, with spatial, slow-time, and channel dimensions. To demonstrate feasibility of the approach, these methods are applied to simulated and *in vivo* liver data.

II. Theory

A. Equations

For clarity, we adopt the following mathematical notation.

1) Scalars are written using standard letters (a, b, N, M).
2) Vectors are written using bold lowercase letters ($\mathbf{a}$, $\mathbf{b}$).
3) 2-D matrices are written as bold uppercase letters ($\mathbf{A}$, $\mathbf{B}$).
4) 3-D matrices (tensors) are written as bold scripts ($\boldsymbol{\mathcal{A}}$, $\boldsymbol{\mathcal{B}}$).

Within mathematical descriptions, Greek lowercase symbols indicate scalars and uppercase indicate symbols indicate matrices. Scalar elements are denoted using subscripts, e.g., the (i, j)-element of $\mathbf{A}$ is a_{ij} and the (i, j, k)-element of $\boldsymbol{\mathcal{B}}$ is b_{ijk}.

B. Doppler Data

In conventional PD processing, filtering is applied to beamformed radio frequency data, which is composed of Z axial samples, X lateral samples, and N slow-time frames. To perform SVD, the beamformed data is often reshaped into Casorati form, combining the axial and lateral spatial dimensions to yield the 2-D matrix $\boldsymbol{X} \in \mathbb{C}^{M\times N}$, where $M \overset{\text{def}}{=} XZ$ [14].

We propose using the HOSVD to filter aperture data. "Aperture data" refers to the delayed channel data after synthetic transmit focusing, prior to the beam sum. This data is composed of Z axial samples, X lateral samples, N slow-time frames, and K channels. Combining the spatial samples in a Casorati form, the aperture data is represented as a 3-D matrix, $\boldsymbol{\mathcal{X}} \in \mathbb{C}^{M\times N\times K}$.

C. Singular Value Decomposition

Conventionally, the SVD of the beamformed data matrix $\boldsymbol{X} \in \mathbb{C}^{M\times N}$ is given by

$$\boldsymbol{X} = \boldsymbol{U}\boldsymbol{S}\boldsymbol{V}' \tag{1}$$

where unitary matrices $\boldsymbol{U} \in \mathbb{C}^{M\times M}$ and $\boldsymbol{V} \in \mathbb{C}^{N\times N}$ contain the spatial and temporal singular vectors, respectively. The matrix, $\boldsymbol{S} \in \mathbb{R}^{M\times N}$, contains the corresponding singular values along the diagonal.

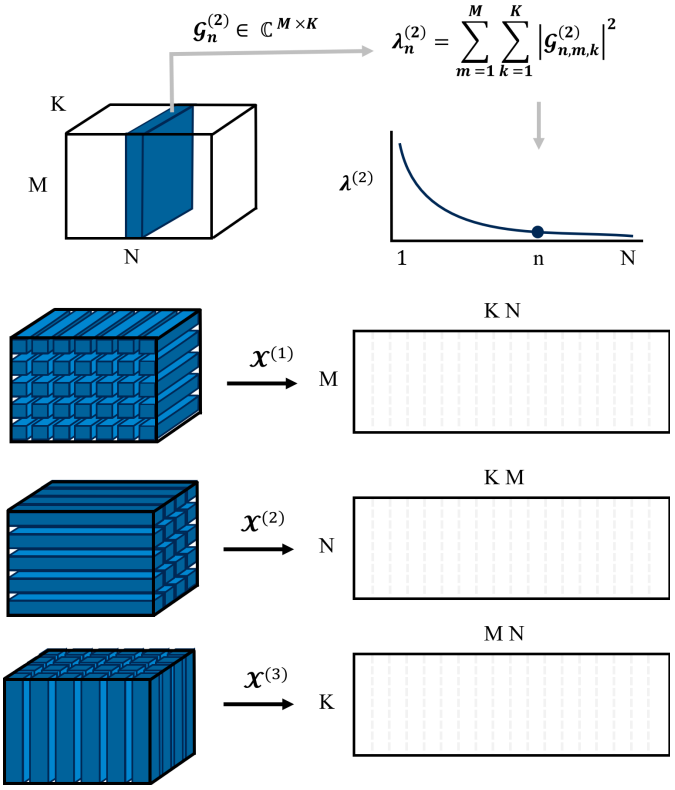

Fig. 1. Computation of the mode-2 eigenvalues from the HOSVD core tensor, $\mathcal{G}$ (top). Mode-n unfoldings of the data tensor, $\mathcal{X}$, used to compute eigenvectors (bottom).

D. Higher Order Singular Value Decomposition

The HOSVD is a generalization of the SVD and a special case of the Tucker decomposition [30]. The HOSVD of the 3-D aperture data tensor $\boldsymbol{\mathcal{X}} \in \mathbb{C}^{M\times N\times K}$ is given by

$$\boldsymbol{\mathcal{X}} = \mathcal{G} \times_1 \boldsymbol{U} \times_2 \boldsymbol{V} \times_3 \boldsymbol{W} \tag{2}$$

where $\times_n$ indicates the mode-n product [30]. The mode-n product, $\mathcal{G} \times_n \boldsymbol{U}$, is equivalent to the multiplication of the matrix and the mode-n unfolding of the tensor, e.g., $\boldsymbol{U}\mathcal{G}_{(n)}$. The unfolded matrix, denoted by the subscript $\boldsymbol{\mathcal{X}}_{(n)}$, is the 2-D matrix representation of the data formed by fixing one dimension and combining the other dimensions, as depicted in Fig. 1 [31].

As shown in Fig. 2, HOSVD yields a core tensor, $\mathcal{G} \in \mathbb{C}^{M\times N\times K}$ and three unitary matrices, namely, the spatial singular vectors, $\boldsymbol{U} \in \mathbb{C}^{M\times M}$, the temporal singular vectors, $\boldsymbol{V} \in \mathbb{C}^{N\times N}$, and the channel singular vectors, $\boldsymbol{W} \in \mathbb{C}^{K\times K}$. In practice, the singular vector matrices are computed from the mode-n unfoldings of $\boldsymbol{\mathcal{X}}$. The unfolded matrix is used to produce a covariance matrix, $\boldsymbol{R}$, from which the singular vector matrix is obtained through eigen decomposition

$$\boldsymbol{R}_M = \boldsymbol{\mathcal{X}}_{(1)}\boldsymbol{\mathcal{X}}_{(1)}^{\mathrm{T}} = \boldsymbol{U}\boldsymbol{\Lambda}_{\mathrm{M}}\boldsymbol{U}^{\mathrm{T}} \tag{3}$$

$$\boldsymbol{R}_N = \boldsymbol{\mathcal{X}}_{(2)}\boldsymbol{\mathcal{X}}_{(2)}^{\mathrm{T}} = \boldsymbol{V}\boldsymbol{\Lambda}_{\mathrm{N}}\boldsymbol{V}^{\mathrm{T}} \tag{4}$$

$$\boldsymbol{R}_K = \boldsymbol{\mathcal{X}}_{(3)}\boldsymbol{\mathcal{X}}_{(3)}^{\mathrm{T}} = \boldsymbol{W}\boldsymbol{\Lambda}_{\mathrm{K}}\boldsymbol{W}^{\mathrm{T}}. \tag{5}$$

The set of mode-n singular values, $\boldsymbol{\lambda}^{(n)}$, are computed as the Frobenius norms of the core tensor, $\mathcal{G}$. This can be written as

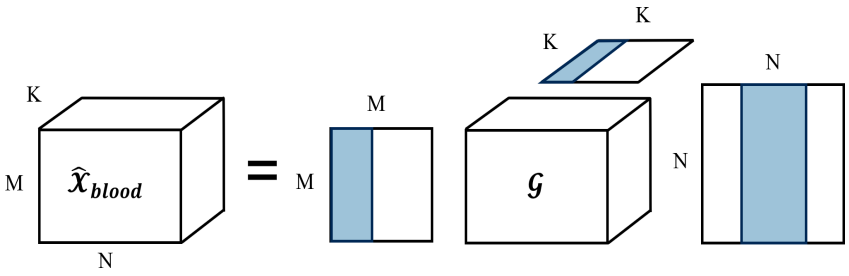

Fig. 2. HOSVD of the data tensor, $\mathcal{X}$, yields the core tensor $\mathcal{G}$ and three eigenvector matrices corresponding to temporal, spatial, and aperture dimensions.

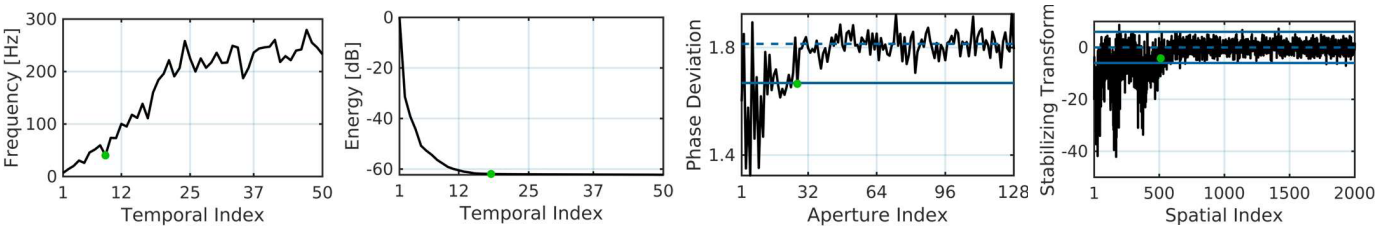

Fig. 3. Features used for HOSVD cutoff selection (green marker) include temporal singular vector mean frequency, temporal singular value magnitude, aperture singular vector phase deviation, and spatial singular vector amplitude characteristics (left to right).

follows:

$$\lambda_m^{(1)} = \sum_{n=1}^{N}\sum_{k=1}^{K} |g_{m,n,k}|^2 \tag{6}$$

$$\lambda_n^{(2)} = \sum_{m=1}^{M}\sum_{k=1}^{K} |g_{m,n,k}|^2 \tag{7}$$

$$\lambda_k^{(3)} = \sum_{m=1}^{M}\sum_{n=1}^{N} |g_{m,n,k}|^2. \tag{8}$$

III. Filter Design

HOSVD and SVD filtering involve a similar process characterized by (1) decomposition of the Doppler data, (2) classification of the dominant signal type contained in each orthogonal component, and (3) rejection of the components corresponding to clutter and noise. We define the HOSVD filter rejection band using four cutoffs, $\{c_{t1}, c_{t2}, c_a,$ and $c_s\}$, obtained using the following classification scheme. The features used to determine the cutoffs are shown in Fig. 3.

A. Temporal Domain Classification

Two cutoffs are defined in the temporal domain. The lower cutoff is used to reject clutter, which typically exhibits a large magnitude and low mean Doppler frequency. The upper cutoff is defined to reject noise, which typically is clustered in the final singular values.

As shown in Fig. 4, the spectral content of the temporal singular vectors is nearly symmetric across the positive and negative frequencies. For each singular vector, the mean frequency was estimated from the power spectral density [11], [14]. The lower cutoff, c_{t1}, is chosen to be the point where the mean singular vector frequency exceeds a specified cutoff frequency. The cutoff frequency is selected to reject components that contain the clutter signal. The frequency

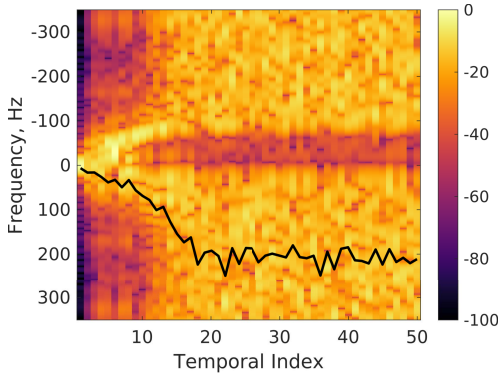

Fig. 4. Power spectral density of temporal singular vectors. The black line indicates the weighted mean frequency.

distribution and quantity of clutter-bearing components are influenced by imaging conditions such as the presence of motion and the clutter-to-blood ratio [13].

For noise rejection, the upper cutoff is determined in two steps, as presented by Song *et al.* [15]. First, a precutoff is defined by fitting the Doppler frequencies to a sigmoid function to find the noise transition point. Second, a linear fit is applied to the singular values after the precutoff point, as the singular value magnitude of noise is expected to follow the Marčenko–Pastur distribution [15], [32]. The upper cutoff, c_{t2}, is chosen as the point where the singular values deviate from this line.

B. Aperture Domain Classification

Several aperture domain features have been leveraged by adaptive beamformers, including coherence [33], [34], frequency [35], and phase disparity [36]. Further, a limited number of aperture domain SVD studies have demonstrated that

singular value magnitude [28] and singular vector frequency [29] can be used for classification.

Here we propose a single cutoff that uses the phase characteristics of the complex singular vectors. As described by Camacho *et al.* [36], the phase disparity across the aperture may be used to discriminate between echoes from the focal zone and echoes from other locations. Synthetic aperture focusing achieves uniform focusing over the entire field of view, such that ON-axis signals are phase aligned, exhibiting low deviation. In comparison, OFF-axis clutter signals and additive white noise will produce high measures of deviation.

Specifically, the phase of additive white noise can be modeled as a uniform distribution between $-\pi$ and π, with a standard deviation of $(\pi/\sqrt{3})$. Therefore, we computed the standard deviation of the phase for each aperture domain singular vector. The aperture cutoff, c_a, is determined by finding the point where the standard deviation of the phase plateaus to $(\pi/\sqrt{3})$.

In application, a confidence interval for the spatial cutoff was determined empirically. The standard deviation was measured from 100 000 realizations of uniformly distributed random values of length N. The 2.5 and 97.5 percentiles were used to compute a 95% confidence interval. If the measured phase exceeded the upper confidence interval bound, the signal likely crossed the $-\pi$ to π phase boundary, so auxiliary phases were computed, as done by Camacho *et al.* [36]. The aperture cutoff, c_a, was defined as the last point where the measured phase fell below the lower confidence interval bound.

C. Spatial Domain Classification

In the spatial domain, we leverage the amplitude characteristics of the singular vectors. Singular vectors containing noise can be modeled as zero-mean complex Gaussian signals, $\sim N(0, \sigma^2)$. The amplitude component of these singular vectors is therefore characterized by the Nakagami distribution with shape and scale parameters of $m = 1$ and $w = 2\sigma^2$.

The Nakagami shape parameter, m, has been used to characterize envelope statistics of backscattered echoes, as the Nakagami distribution encompasses pre-Rayleigh ($m < 1$), Rayleigh ($m = 1$), and Rician ($m > 1$) statistics [37], [38]. The inverse normalized variance estimator (INV) is a common technique for estimating the Nakagami shape parameter [39], [40]. The INV estimator is $\sqrt{N}$-consistent and asymptotically unbiased, defined as

$$\hat{m}_{\mathrm{INV}} = \frac{\left(E\left[A^2\right]\right)^2}{E\left[A^4\right] - \left(E\left[A^2\right]\right)^2}. \tag{9}$$

As a result, we can define a stabilizing transform which converges to a zero-mean Gaussian random variable

$$s = \sqrt{N}(\hat{m}_{\mathrm{INV}} - m) \rightarrow N\left(0, \sigma^2_{\mathrm{INV}}\right) \tag{10}$$

with an asymptotic variance of

$$\sigma^2_{\mathrm{INV}} = 2m(m+1). \tag{11}$$

The stabilizing transform parameter, s, is to be computed for every spatial singular vector. Finally, the spatial cutoff, c_s, is defined as the point where s falls within $\pm 3\sigma_{\mathrm{INV}}$. In practice, a 5-point moving average was first applied to the stabilizing transform parameter, to reduce spurious outliers.

D. Clutter Rejection and Power Estimation

Filtering is performed by reducing or zeroing the clutter-dominant components. Therefore, we define the blood core tensor, $\hat{\mathcal{G}}$, as

$$\hat{g}_{m,n,k} = \begin{cases} 0, & \text{for } c_s \leq m \leq M \\ 0, & \text{for } c_a \leq n \leq N \\ 0, & \text{for } k \leq c_{t1} \text{ and } \geq c_{t2} \\ g_{m,n,k}, & \text{otherwise} \end{cases} \tag{12}$$

and filtered data set as

$$\hat{\boldsymbol{\mathcal{X}}} = \hat{\boldsymbol{G}} \times_1 \boldsymbol{U} \times_2 \boldsymbol{V} \times_3 \boldsymbol{W}. \tag{13}$$

Finally, the beamsum and power estimation are performed, yielding the PD image, $\boldsymbol{P_{HOSVD}}$. Fig. 5 depicts an example of the benefit of multidimensional clutter rejection, showing that the greatest detection of the ON-axis blood flow signal is achieved using temporal, spatial, and aperture domain cutoffs.

IV. Methods

Processing and analysis were performed in MATLAB (version R2018b, MathWorks, Natick, MA, USA). Beamforming was implemented using the UltraSound ToolBox (v2.1) [41]. The TensorLab (v3.0) function mlsvd was used for HOSVD [42]. All PD images are shown on a dynamic range normalized to the maximum intensity of the image.

A. Performance Metrics

We compare the HOSVD filter to: (1) a conventional SVD filter applied to the radio frequency data and (2) a novel SVD filter applied to the mode-3 unfolding (e.g., frames $\times$ space $*$ channels) of the aperture data. "Gold standard" PD images were formed using these methods, denoted $\boldsymbol{P_{SVD}}$ and $\boldsymbol{P_{SVD-a}}$, respectively.

The blood flow detection performance was assessed using a receiver operating characteristic (ROC) curve analysis, similar to Chee and Yu [43]. ROC curves were generated by plotting the true positive rate against the false positive rate, measured over a set of thresholds. The true positive rate was defined as the fraction of blood pixels that exceeded the threshold value, and the false positive rate was defined as the fraction of tissue pixels that exceeded the threshold value. The thresholds were postfilter Doppler power values, swept between the minimum and maximum Doppler power in 0.2-dB increments. The area under the ROC curve (AUC) was used to quantify how well the blood flow was distinguished from the background.

Further, the image quality was measured in terms of the contrast, defined as follows:

$$\text{Contrast} = 10 * \log10\left(\frac{\bar{P}_{\text{blood}}}{\bar{P}_{\text{backgroud}}}\right) \tag{14}$$

and the contrast-to-noise ratio (CNR)

$$\text{CNR} = 10 * \log10\left(\frac{\bar{P}_{\text{blood}} - \bar{P}_{\text{background}}}{\sigma_{\text{background}}}\right). \tag{15}$$

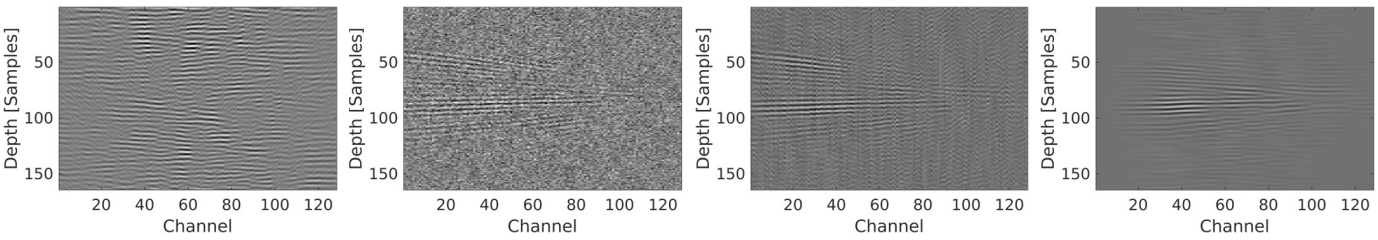

Fig. 5. Examples of delayed channel data with various levels of clutter rejection filtering. (1) Unfiltered data, (2) temporal filtering only, (3) temporal and spatial filtering, and (4) temporal, spatial, and aperture filtering (left to right).

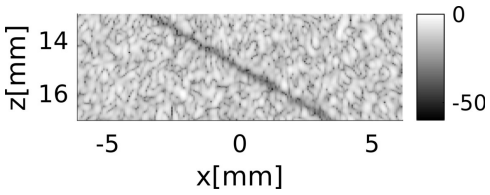

Fig. 6. Sample B-mode of simulated vessel phantom shown on a 60-dB scale.

B. Simulation Design

A simulation study was conducted using Field II [44], [45]. A 2×3 cm^2 tissue phantom was designed with a 0.4-mm vessel angled 60° relative to the probe. Blood scatterers were perfused in a parabolic velocity profile, with a peak velocity of 10 mm/s.

To simulate realistic clutter, bulk motion was applied to the tissue and blood scatterers. Five independent motion profiles were obtained by averaging 2-D displacement estimates [46] from tissue mimicking phantoms. The five tissue phantoms were composed of a polyvinyl alcohol (PVA)-graphite mixture [8] and acquired using an L12-4 probe held freely by a sonographer. The phantom acquisition was performed using probe parameters similar to the simulation ($f_0 = 7.813$ MHz and $f_s = 31.24$ MHz) and the same plane wave acquisition sequence.

Five independent simulation realizations were generated using the five motion profiles. For each simulation, the tissue and blood channel data were simulated separately, and normally distributed random noise was used to simulate electronic noise. The data were combined using a -40-dB blood-to-tissue ratio and a -45-dB noise-to-tissue ratio. Five phantoms were generated for independent speckle and displacement realizations. A sample B-mode is shown in Fig. 6.

A linear probe was modeled using the parameters shown in Table I. Channel data was acquired using an ultrafast plane wave sequence composed of 13 plane waves evenly spaced between $-2.7°$ and 2.7°. PWSF was applied to achieve uniform focusing [1], yielding a net PRF of 700 Hz. PD images were formed from a 4×13 mm^2 patch (164×64 samples) of simulated data.

C. Simulation Experimental Setup

1) Optimal Performance: To assess the optimal performance of the filter, a set of PD images were formed by manually defining the HOSVD cutoffs in a bounded grid search over the ranges depicted in Table II. Since the optimal contrast, CNR and AUC may correspond to unique cutoff choices, each performance metric was optimized separately. The reference SVD filters were manually tuned over the c_{t1} and c_{t2} ranges. Ensembles of 50 frames were used.

TABLE I
FIELD II SIMULATION PARAMETERS

Parameter	Value
f_0	7.813 MHz
Bandwidth	65%
f_s	78.13 MHz
Element Number	128
Element Width	0.1703 mm
Element Pitch	0.1953 mm
Sound Speed	1540 m/s

TABLE II
OPTIMAL PERFORMANCE STUDY CUTOFF RANGES

Parameter	Min	Max	Increment
c_{t1}	1	$K-2$	2
c_{t2}	$c_{t1}+2$	K	2
c_a	8	64	8
c_s	400	1900	300

2) Classifier Performance: Classifier performance was assessed by comparing the results of the manually tuned study to PD images formed using the HOSVD cutoffs obtained using the classifier described in Section III.

The spatial and aperture domain cutoffs were determined using the theoretical cutoff points, e.g., when the phase deviation plateaued at $(\pi/\sqrt{3})$ and when the stabilizing transform parameter plateaued at $\pm 3\sigma^2_{\text{INV}}$. The lower temporal cutoff, defined as a cutoff frequency, was the only bound that needed to be parameterized. The temporal cutoff frequency was tuned between 2 and 100 Hz, in 2-Hz increments. Ensembles of 50 frames were used.

3) Short Ensemble Performance: To assess the value of using HOSVD filtering for PD imaging using relatively short ensembles, images were additionally formed using ensembles of 16 and 25 frames. The same classifier parameterization was used; however, the temporal cutoff frequency was tuned between 2 and 200 Hz, in 2-Hz increments. The extended

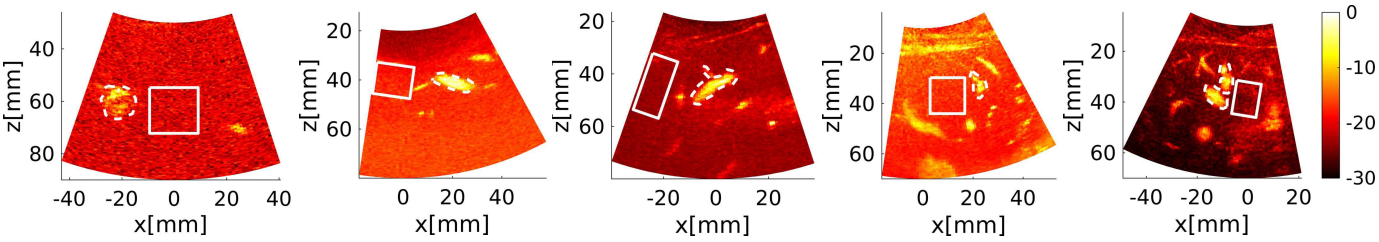

Fig. 7. Blood (dashed) and background (solid) regions of interest used for human *in vivo* performance assessment. PD images formed using a conventional SVD filter are shown on a 30-dB scale.

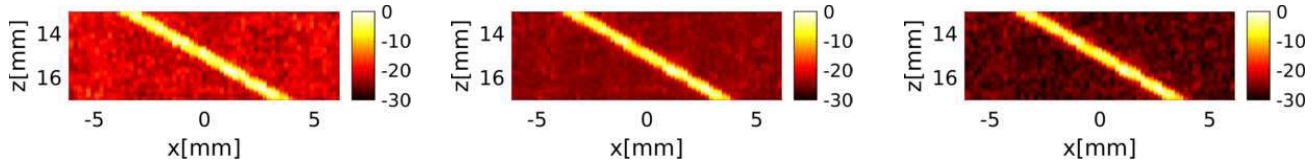

Fig. 8. Sample PD images obtained using SVD, SVD-a, and HOSVD. Images correspond to the results from the classifier-generated cutoff study that produced the highest contrast for a single simulation case.

frequency range was used as shorter ensembles result in temporal singular vectors with more broadband frequency content, which increases the mean frequency.

D. In Vivo Study

Efficacy was further demonstrated *in vivo* using a small pilot study of liver imaging data acquired from a healthy adult male subject. Five data sets were obtained in compliance with Vanderbilt's Institutional Review Board (IRB) protocol.

Channel data was acquired using a C5-2 probe on a Verasonics research system (Verasonics Inc., Kirkland, WA, USA), with a sequence composed of nine angled plane wave transmits evenly spaced from $-4°$ to $4°$. The pulse was designed with a f_0 of 4.167 MHz and f_s of 16.68 MHz. PWSF was applied, yielding a net PRF of 600 Hz.

1) Image Quality: PD images were formed using ensembles of 50 frames. Since global processing was used, depth-dependent effects such as attenuation and gain may confound accurate estimation of the Nakagami parameters [37]. To overcome this constraint, the power of each singular vector amplitude was normalized through depth when computing the stabilizing transform parameter. For each data set, a single region of 1299 axial samples and 64 lateral samples was processed. The temporal cutoff frequency was tuned between 2 and 200 Hz, in 2-Hz increments. Image quality was measured in terms of contrast and CNR using manually segmented regions of interest, as shown in Fig. 7. To assess the sensitivity of each filter toward the temporal cutoff frequency, the robustness was measured in terms of contrast loss relative to the highest achievable contrast for each data set. This was measured as $1-(|\text{Contrast}-\text{Contrast}_{\max}|)/(\text{Contrast}_{\max})$, using the nonlog compressed contrast values.

2) Computational Complexity: The computational cost of HOSVD filtering is more demanding than conventional SVD filtering. The HOSVD and SVD-a filters are both applied to delayed channel data, which inherently increases the memory demand by the size of the channel count in comparison to conventional SVD filtering which is applied to beamformed radio frequency data.

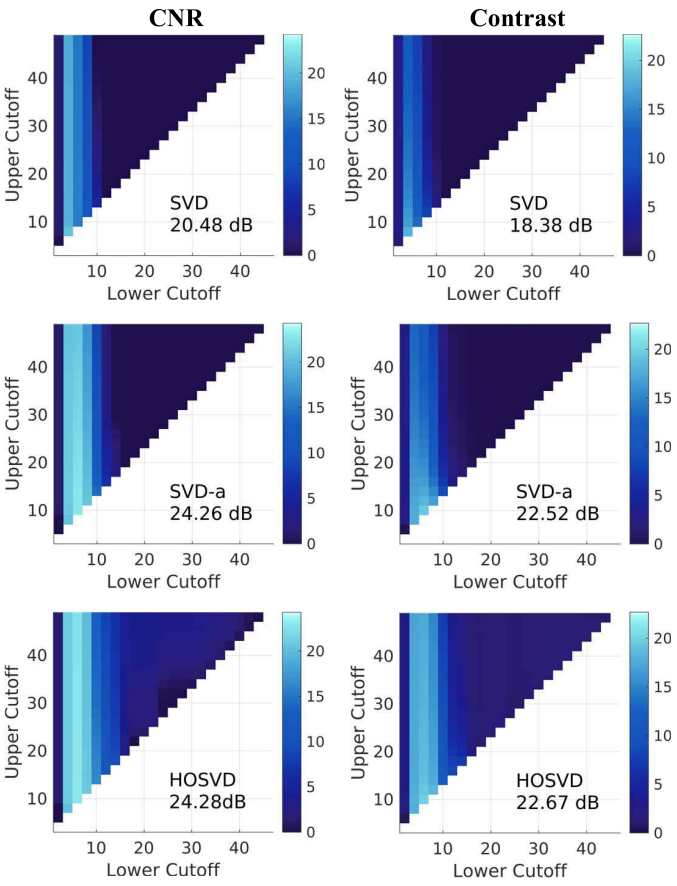

Fig. 9. Depiction of the optimal performance study grid search. CNR (left) and contrast (right) results shown on a dB scale for $\boldsymbol{P}_{SVD}$ (top), $\boldsymbol{P}_{SVD-a}$ (middle), and $\boldsymbol{P}_{HOSVD}$ (bottom) as a function of the lower and upper temporal cutoffs. The HOSVD results depict the highest values obtained over the spatial and aperture ranges. The highest achieved image quality for each method is shown in bottom corner.

The computational complexity of SVD is often approximated as $\mathcal{O}(mn^2)$ for a matrix with dimensions $m > n$.

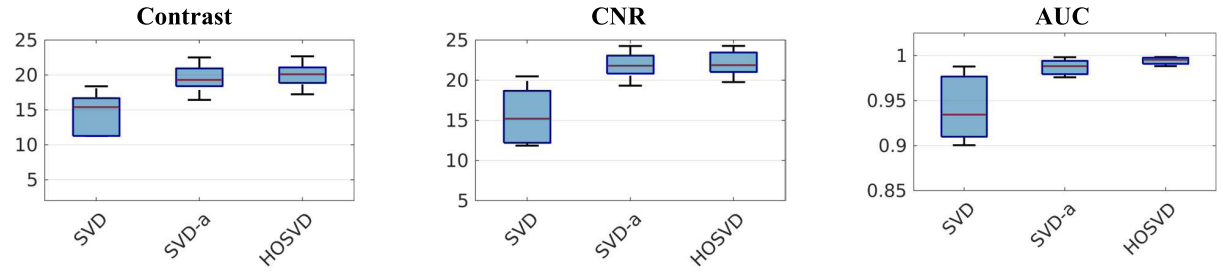

Fig. 10. Simulation results for the optimal performance study. Contrast and CNR are shown on a dB scale.

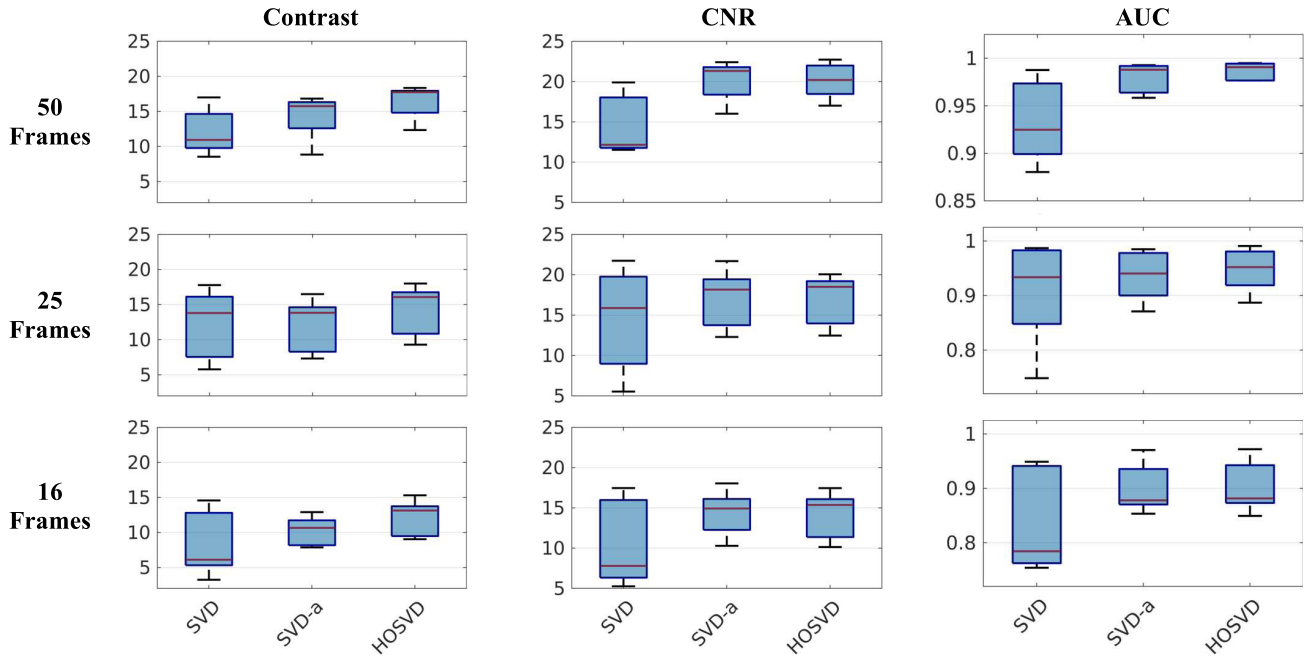

Fig. 11. Image quality results for ensembles of 50 (top), 25 (center), and 16 (bottom) using the classifier-generated cutoffs. Contrast (dB), CNR (dB), and AUC (left to right).

As a tensor method, the computational complexity of HOSVD is greater, although truncated methods and efficient approximation methods have been developed. The HOSVD of a 3-D tensor with dimensions $[k, m, n]$ involves three separate SVDs to obtain the singular vector matrices. We estimate that HOSVD would therefore be associated with a baseline computational complexity of roughly $[\mathcal{O}(mnk^2) + \mathcal{O}(knm^2) + \mathcal{O}(kmn^2)]$. However, the absolute computational throughput would depend on various factors, including the processing system, available memory, and decomposition algorithm.

The time expense of the different decomposition methods was evaluated using the five *in vivo* data sets with varied parameterization. We measured the total serial run time to perform each decomposition in MATLAB (The Mathworks Inc., Natick) on a desktop computer running dual Intel Xeon E5-3643 v4 CPUs at 3.40 GHz with 6 cores each. The computation time across each run was measured using the built-in MATLAB tic and toc commands.

For benchmarking, transmit beamforming was applied to each *in vivo* data set, yielding a tensor with dimensions $[M \times N \times K]$ corresponding to spatial samples, channels, and frames. The HOSVD computation time was recorded as the time to decompose the full tensor. We assessed the time to perform a standard HOSVD using the function mlsvd. The SVD-a computation time was recorded as the time to perform an SVD on the unfolded matrix with dimensions of $[MN \times K]$. Finally, the conventional SVD computation time was measured as the time to perform an SVD on the beamformed matrix with dimensions of $[M \times K]$, obtained by summing over the tensor's channel dimension.

To assess the effects of varied parameterization, we demonstrate the relative effects of: (1) changing the temporal ensemble length between 10 and 50 frames and (2) processing a spatial sample containing between 100 and 500 depth samples. For all cases, 128 channels and 64 lateral samples were used. Plots were formed to depict the effect of varying each parameter while holding the other parameter constant at 50 frames or 500 pixels, respectively.

V. Results and Discussion

A. Simulation Study

The HOSVD clutter filter demonstrated improved performance over the SVD filters in simulation, as depicted in Fig. 8.

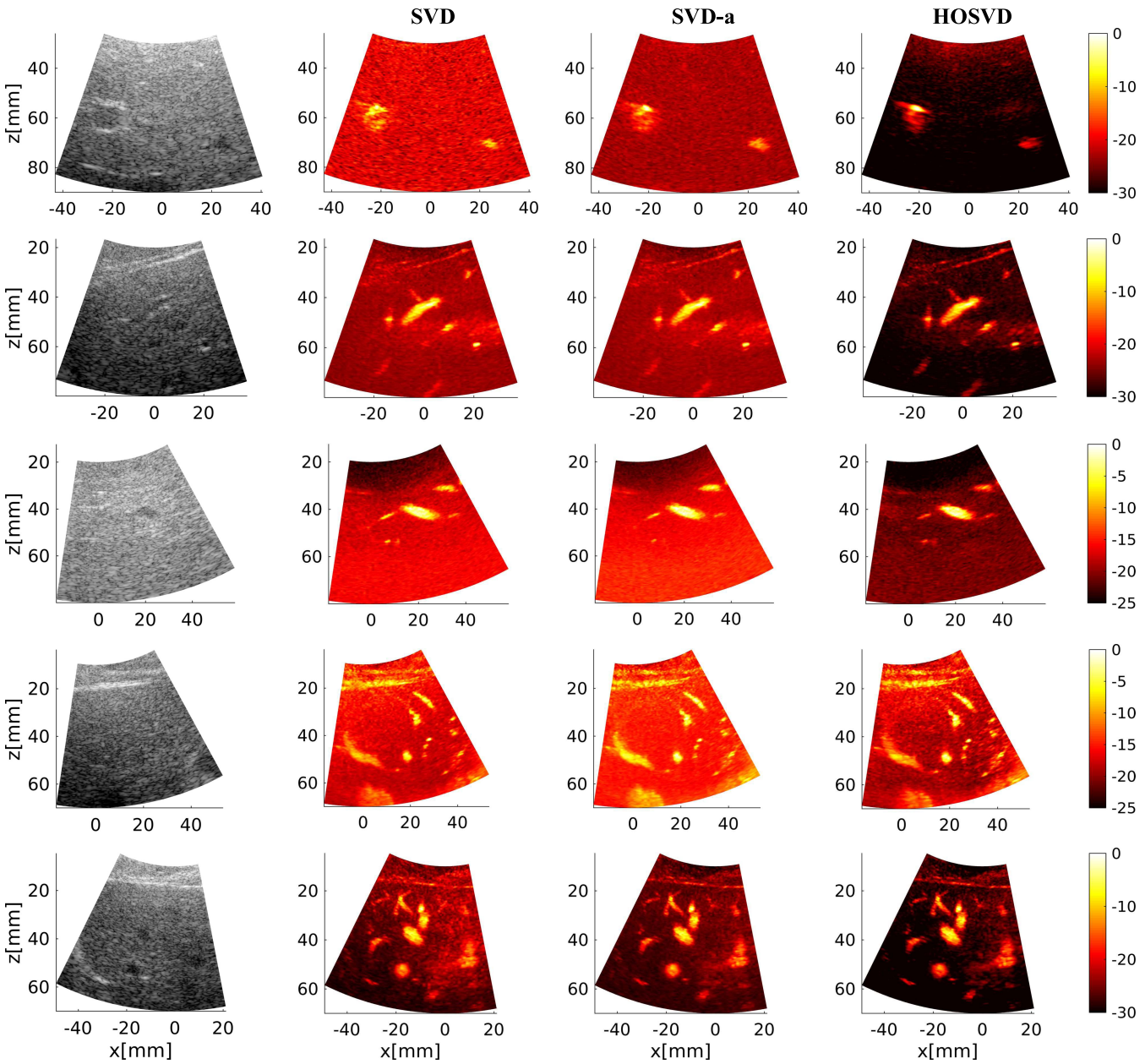

Fig. 12. B-mode, P_{SVD}, P_{SVD-a}, and P_{HOSVD} images depicting peripheral blood flow in a healthy liver. B-mode images are shown on a 60-dB scale. Filtered images display the highest contrast achieved using each filter (left to right).

Result metrics are reported using the mean ± one standard deviation over the five simulated phantoms.

1) Optimal Performance: HOSVD outperformed conventional SVD filtering in an ideal setting, as depicted in Figs. 9 and 10. Using the optimized set of manually tuned cutoffs for each filter, HOSVD produced a maximum contrast of 19.99 ± 1.97 dB, compared to SVD (14.48 ± 3.13 dB) and SVD-a (19.54 ± 2.21 dB). Similarly, HOSVD produced a higher maximum CNR (22.11 ± 1.72 dB versus 15.59 ± 3.7 dB for SVD and 21.88 ± 1.81 dB for SVD-a).

However, an additional key benefit of HOSVD is that it is more robust in nonideal conditions than SVD or SVD-a. Fig. 9 depicts contrast and CNR results across all temporal cutoffs for a single simulated data set. Similar to the findings of Mauldin *et al.* [16], Fig. 9 highlights that errors in threshold choice for SVD and SVD-a can cause substantial loss in image quality. The lower temporal cutoff can have the greatest effect on image quality, as it is a primary means of rejecting ON-axis clutter and the cutoff is operator-dependent. HOSVD is less sensitive to the temporal frequency cutoff choice than SVD and SVD-a, maintaining a broader region of image quality. This is important for clinical imaging scenarios, where factors such as accelerative motion can confound cutoff selection [13].

The differences observed between SVD and SVD-a merit further research but may be explained by several underlying factors. First, we assume that the temporal information provided by the right singular vectors in SVD and SVD-a are comparable. However, scatterer translation is observed differently across the aperture [47], therefore it is reasonable to hypothesize that temporal information may be encoded

differently. In addition, the consistency of basis estimation using sample data matrices is dependent on the ratio between the number of samples and number of observations [48]. Since the temporal singular vectors of SVD-a are derived using a factor equal to the number of channels (K) additional observations, there may be implicit differences between the SVD-a and SVD subspaces.

2) Classifier Performance: The classifier scheme used to generate the HOSVD filter cutoffs demonstrated robust performance in simulation. The PD images generated using the classifier-generated cutoffs produced reasonably similar image quality in comparison to the optimal cutoff case. This result is quantified via the AUC analysis in Fig. 11, where the HOSVD classifier cutoff produced a maximal AUC of 0.987 ± 0.009, in comparison to the optimal cutoff AUC of 0.994 ± 0.004. In comparison, the maximal $\boldsymbol{P_{SVD}}$ and $\boldsymbol{P_{SVD-A}}$ AUC values were measured as 0.933 ± 0.044 and 0.979 ± 0.016. HOSVD produced a maximum contrast of 16.37 ± 2.45 dB, compared to SVD (12.10 ± 3.34 dB) and SVD-a (14.28 ± 3.24 dB).

3) Short Ensemble Performance: Across ensemble sizes, HOSVD remained an effective method for clutter rejection. Fig. 11 shows maximum contrast, CNR, and AUC for ensemble sizes of 16, 25, and 50 frames, respectively. For 16 frames, $\boldsymbol{P_{HOSVD}}$ produced a maximum contrast of 12.07 ± 2.64 dB, compared to $\boldsymbol{P_{SVD}}$ (8.43 ± 4.74 dB) and $\boldsymbol{P_{SVD-a}}$ (10.21 ± 2.12 dB). For 25 frames, $\boldsymbol{P_{HOSVD}}$ produced a maximum contrast of 14.21 ± 3.69 dB, compared to $\boldsymbol{P_{SVD}}$ (12.21 ± 5.06 dB) and $\boldsymbol{P_{SVD-a}}$ (12.05 ± 3.90 dB).

The HOSVD and SVD-a filters have similar tissue rejection performance because they leverage the same temporal singular vectors produced by the unfolded data tensor for tissue classification, as described in Section III-A. However, the HOSVD filter additionally leverages spatial and aperture domain signal suppression, which enables greater rejection of noise and OFF-axis signals. In addition, aside from rank limitations, the spatial and aperture domain signal classification methods are independent of temporal ensemble length. This is supported by Fig. 11, which shows that HOSVD filter consistently yielded contrast gains over the conventional SVD filter, which demonstrates effective clutter rejection despite varied ensemble size. Further, the HOSVD filter consistently yielded a median AUC above 0.85 for varied ensemble lengths indicating that vessel discrimination remained strong. Overall, this demonstrates that HOSVD is robust to ensemble size constraints observed on clinical scanners.

B. In Vivo Study

1) Image Quality Performance: In Vivo: feasibility is demonstrated in liver data, as shown in Fig. 12, which depicts the $\boldsymbol{P_{HOSVD}}$, $\boldsymbol{P_{SVD}}$, and $\boldsymbol{P_{SVD-a}}$ images. As shown in Fig. 13, HOSVD produced greater rejection of clutter and noise, yielding a maximum contrast of 14.15 ± 2.69 dB and maximum CNR of 19.01 ± 3.03 dB. In comparison, the SVD filter produced a contrast of 9.92 ± 2.83 dB and CNR of 14.96 ± 3.15 dB, and the SVD-a filter produced a contrast of 10.49 ± 2.95 dB and CNR of 17.05 ± 3.03 dB. Fig. 14 depicts the effect of overestimation and underestimation of the temporal frequency cutoff, which is manually parameterized. Similar to the findings of Baranger *et al.* [11], threshold estimation error results in decreased image quality for all filters. However, the HOSVD filter retains a higher contrast at nonoptimal cutoff frequencies in comparison to SVD and SVD-a.

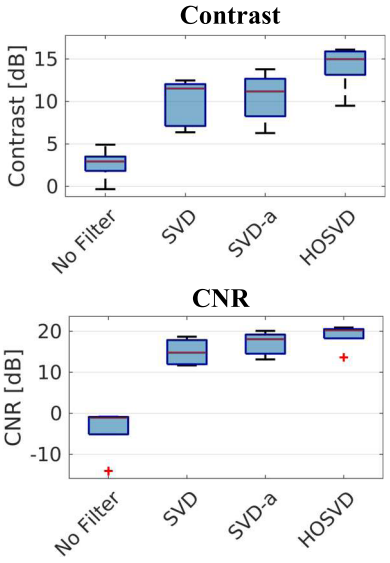

Fig. 13. Image quality results for *in vivo* study. Results are depicted for PD images formed using SVD, SVD-a, and HOSVD filtering. Metrics for a nonfiltered PD image shown for reference.

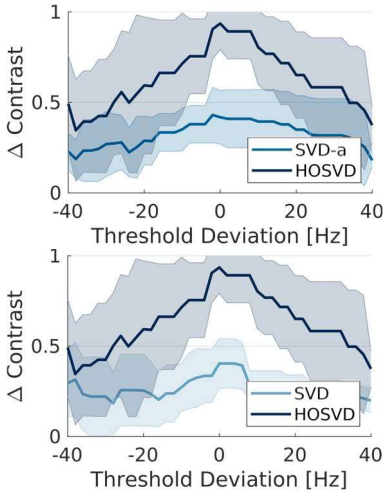

Fig. 14. Effect of overestimation and underestimation of the temporal frequency cutoff on image contrast, shown in terms of relative change in comparison to the maximum achievable contrast.

This pilot study shows that HOSVD filtering can improve visualization of blood flow in clinical imaging scenarios. The HOSVD filter improves contrast, which improves assessment of vasculature through the reduction of clutter and noise. Abdominal ultrasound imaging is associated with higher rates of inadequate clinical visualization and limitations due to poor image quality [49]. Due to improved suppression of noise and clutter, small vasculature is more readily observed with HOSVD filtering in comparison to SVD and SVD-a.

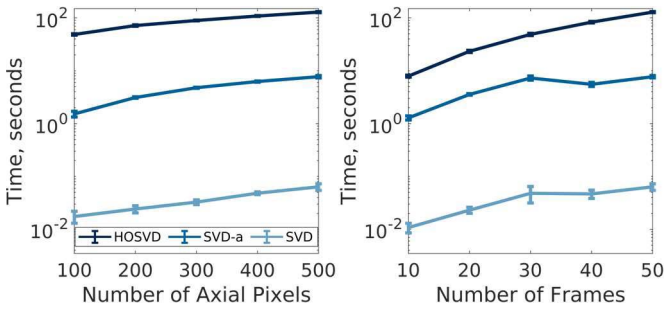

Fig. 15. Computational expense for SVD, SVD-a, and HOSVD with varied spatial (left) and temporal (right) parameterization.

2) Computational Complexity: One drawback of HOSVD filtering is its associated computational complexity. As shown in Fig. 15, the computation time increases at a greater rate with HOSVD in comparison to SVD. This suggests that block-wise, downsampling [24], or projecting [50] may greatly improve HOSVD processing speed. In addition, blockwise processing reduces variation caused by time-gain compensation and depth-dependent effects, which may improve estimation of the Nakagami parameters. Further, performing a truncated HOSVD has been shown to improve computational time without a reduction in filtering performance [26]. For example, a sequentially truncated HOSVD [51] could be parameterized with an adaptive tolerance that is defined using the upper channel cutoff, spatial cutoff, and channel cutoff.

VI. Conclusion

Expanding the dimensionality of clutter rejection filters has substantial opportunity for PD imaging. We demonstrate that leveraging spatial, temporal, and aperture features can enable improved rejection of clutter and noise signals. Further, we show that multidimensional decomposition effectively captures dynamic imaging environments in relatively few samples, which is valuable for clinical contexts.

This work validates a semiautomated multidimensional classifier that operates along spatial, temporal, and aperture extents. The classifier leverages theoretical principles of signal phase and amplitude to reject OFF-axis clutter and noise. These signal features used for classification are likely interchangeable over the different dimensions, as we assume that the noise-bearing components of each dimension are white Gaussian processes. To reject tissue clutter, a frequency-based classifier parameterized by a cutoff frequency is also employed, which is a broadly accepted method within SVD literature [13]. We note that automated approaches to find the lower temporal cutoff have also been proposed, such as computing the minima of the singular value curvature radius [11]. Overall, this semiautomated framework reduces the burden of cutoff parameterization and can improve performance across varied clinical contexts.

Since the HOSVD filter may be used in place of the SVD filter, HOSVD filtering may be used in a variety of imaging applications beyond PD imaging. SVD and other blind source separation filtering techniques have been investigated for several other blood flow imaging applications, including color Doppler [13], contrast-enhanced ultrasound [53], and super resolution imaging [54]. Further, similar blind source separation methods have been examined for tissue imaging applications, such as for minimum variance imaging [4], clutter rejection [5], and noise suppression [6]. HOSVD filtering can also be used concurrently with other postprocessing methods, including morphological filtering or background noise removal [5], [54]. The combination of adaptive clutter filtering and noise suppression algorithms has been shown to yield remarkable improvements in image quality, and we anticipate HOSVD filtering would yield a similar combinatorial benefit.

Additionally, HOSVD filtering may be directly amenable to adaptive beamformers. A number of techniques have been proposed which require clutter rejection filtering of aperture or subaperture data, including coherent flow PD (CFPD) [7], power-preserving coherent flow PD (ppCFPD) [8], short-lag angular coherence (SLAC) [33], and acoustic subaperture processing (ASAP) [6]. A drawback of coherence-based adaptive beamformers is the presence of "dark region artifacts," which manifest due to strong OFF-axis scattering [55]. Since HOSVD filtering can reject OFF-axis contributions, it may effectively mitigate dark region artifacts in adaptive beamforming. Adaptive beamformers have been shown to benefit from synthetic transmit focusing, which aligns with the assumption of low phase dispersion for the aperture domain classifier. Techniques that use a fixed transmit focus will exhibit greater phase dispersion away from the focal point, which may degrade performance of the phase-based classifier.

Further, we demonstrated the efficacy of HOSVD filtering for visualization of vasculature in the liver, which suggests that HOSVD filtering is well suited for deeper clinical imaging applications. Clinical visualization of low-velocity blood flows and deep imaging targets are frequently limited by body habitus [49]. Future work will assess the combinatorial benefits of using HOSVD filtering with other advanced processing methods, such as adaptive beamforming or motion correction, to visualize low-velocity blood flow in liver lesions. A reliable assessment mechanism of lesion blood flow would improve therapeutic evaluation and clinical outcomes.

In this work, we demonstrate that HOSVD may be used for clutter rejection in a scheme in which contiguous blocks of clutter-dominant components are removed. However, several studies have demonstrated that various imaging conditions may incur subspace overlap, in which tissue and blood features are not separately contained [5], [12], [52]. We anticipate that further study on the selective rejection of indices within the core tensor, $\mathcal{G}$, could produce a clutter rejection filter with even greater efficacy.

Overall, we present a methodology for clutter rejection filtering using a HOSVD filter. The proposed technique effectively overcomes the subspace separation limitations of SVD for short ensembles, achieving greater suppression of clutter and noise without loss of blood flow sensitivity. The novel classification scheme additionally considers features of aperture domain data which have not previously been studied in the context of clutter filtering. Demonstration of the proposed HOSVD filter for *in vivo* visualization of small vasculature demonstrates its potential for clinical translation.

ACKNOWLEDGMENT

The authors would like to thank the staff of the Vanderbilt University Advanced Computing Center for Research and Education (ACCRE) computing resource and the contributors to the UltraSound ToolBox.

REFERENCES

[1] G. Montaldo, M. Tanter, J. Bercoff, N. Benech, and M. Fink, "Coherent plane-wave compounding for very high frame rate ultrasonography and transient elastography," *IEEE Trans. Ultrason., Ferroelectr., Freq. Control*, vol. 56, no. 3, pp. 489–506, Mar. 2009, doi: 10.1109/TUFFC.2009.1067.

[2] E. Mace, G. Montaldo, B.-F. Osmanski, I. Cohen, M. Fink, and M. Tanter, "Functional ultrasound imaging of the brain: Theory and basic principles," *IEEE Trans. Ultrason., Ferroelectr., Freq. Control*, vol. 60, no. 3, pp. 492–506, Mar. 2013, doi: 10.1109/TUFFC.2013.2592.

[3] J. Tierney, J. Baker, A. Borgmann, D. Brown, and B. Byram, "Non-contrast power Doppler ultrasound imaging for early assessment of trans-arterial chemoembolization of liver tumors," *Sci. Rep.*, vol. 9, no. 1, p. 13020, Dec. 2019, doi: 10.1038/s41598-019-49448-8.

[4] C. Huang, P. Song, P. Gong, J. D. Trzasko, A. Manduca, and S. Chen, "Debiasing-based noise suppression for ultrafast ultrasound microvessel imaging," *IEEE Trans. Ultrason., Ferroelectr., Freq. Control*, vol. 66, no. 8, pp. 1281–1291, Aug. 2019, doi: 10.1109/TUFFC.2019.2918180.

[5] P. Song, A. Manduca, J. D. Trzasko, and S. Chen, "Noise equalization for ultrafast plane wave microvessel imaging," *IEEE Trans. Ultrason., Ferroelectr., Freq. Control*, vol. 64, no. 11, pp. 1776–1781, Nov. 2017, doi: 10.1109/TUFFC.2017.2748387.

[6] A. Stanziola, C. H. Leow, E. Bazigou, P. D. Weinberg, and M.-X. Tang, "ASAP: Super-contrast vasculature imaging using coherence analysis and high frame-rate contrast enhanced ultrasound," *IEEE Trans. Med. Imag.*, vol. 37, no. 8, pp. 1847–1856, Aug. 2018, doi: 10.1109/TMI.2018.2798158.

[7] Y. L. Li and J. J. Dahl, "Coherent flow power Doppler (CFPD): Flow detection using spatial coherence beamforming," *IEEE Trans. Ultrason., Ferroelectr., Freq. Control*, vol. 62, no. 6, pp. 1022–1035, Jun. 2015, doi: 10.1109/TUFFC.2014.006793.

[8] K. Ozgun, J. Tierney, and B. Byram, "A spatial coherence beamformer design for power Doppler imaging," *IEEE Trans. Med. Imag.*, vol. 39, no. 5, pp. 1558–1570, May 2020, doi: 10.1109/TMI.2019.2953657.

[9] Y. L. Li and J. J. Dahl, "Angular coherence in ultrasound imaging: Theory and applications," *J. Acoust. Soc. Amer.*, vol. 141, no. 3, pp. 1582–1594, Mar. 2017, doi: 10.1121/1.4976960.

[10] P. Song *et al.*, "Accelerated singular value-based ultrasound blood flow clutter filtering with randomized singular value decomposition and randomized spatial downsampling," *IEEE Trans. Ultrason., Ferroelectr., Freq. Control*, vol. 64, no. 4, pp. 706–716, Apr. 2017, doi: 10.1109/TUFFC.2017.2665342.

[11] J. Baranger, B. Arnal, F. Perren, O. Baud, M. Tanter, and C. Demene, "Adaptive spatiotemporal SVD clutter filtering for ultrafast Doppler imaging using similarity of spatial singular vectors," *IEEE Trans. Med. Imag.*, vol. 37, no. 7, pp. 1574–1586, Jul. 2018, doi: 10.1109/TMI.2018.2789499.

[12] M. Bayat and M. Fatemi, "Concurrent clutter and noise suppression via low rank plus sparse optimization for non-contrast ultrasound flow Doppler processing in microvasculature," in *Proc. IEEE Int. Conf. Acoust., Speech Signal Process. (ICASSP)*, Calgary, AB, Canada, Apr. 2018, pp. 1080–1084, doi: 10.1109/ICASSP.2018.8461638.

[13] A. Yu and L. Lovstakken, "Eigen-based clutter filter design for ultrasound color flow imaging: A review," *IEEE Trans. Ultrason., Ferroelectr., Freq. Control*, vol. 57, no. 5, pp. 1096–1111, May 2010, doi: 10.1109/TUFFC.2010.1521.

[14] C. Demene *et al.*, "Spatiotemporal clutter filtering of ultrafast ultrasound data highly increases Doppler and fUltrasound sensitivity," *IEEE Trans. Med. Imag.*, vol. 34, no. 11, pp. 2271–2285, Nov. 2015, doi: 10.1109/TMI.2015.2428634.

[15] P. Song, A. Manduca, J. D. Trzasko, and S. Chen, "Ultrasound small vessel imaging with block-wise adaptive local clutter filtering," *IEEE Trans. Med. Imag.*, vol. 36, no. 1, pp. 251–262, Jan. 2017, doi: 10.1109/TMI.2016.2605819.

[16] F. W. Mauldin, D. Lin, and J. A. Hossack, "The singular value filter: A general filter design strategy for PCA-based signal separation in medical ultrasound imaging," *IEEE Trans. Med. Imag.*, vol. 30, no. 11, pp. 1951–1964, Nov. 2011, doi: 10.1109/TMI.2011.2160075.

[17] M. Bayat, M. Fatemi, and A. Alizad, "Background removal and vessel filtering of noncontrast ultrasound images of microvasculature," *IEEE Trans. Biomed. Eng.*, vol. 66, no. 3, pp. 831–842, Mar. 2019, doi: 10.1109/TBME.2018.2858205.

[18] A. Heimdal and H. Torp, "Ultrasound Doppler measurements of low velocity blood flow: Limitations due to clutter signals from vibrating muscles," *IEEE Trans. Ultrason., Ferroelectr., Freq. Control*, vol. 44, no. 4, pp. 873–881, Jul. 1997, doi: 10.1109/58.655202.

[19] A. P. Kadi and T. Loupas, "On the performance of regression and step-initialized IIR clutter filters for color Doppler systems in diagnostic medical ultrasound," *IEEE Trans. Ultrason., Ferroelectr., Freq. Control*, vol. 42, no. 5, pp. 927–937, Sep. 1995, doi: 10.1109/58.464825.

[20] S. Bjaerum, H. Torp, and K. Kristoffersen, "Clutter filters adapted to tissue motion in ultrasound color flow imaging," *IEEE Trans. Ultrason., Ferroelectr., Freq. Control*, vol. 49, no. 6, pp. 693–704, Jun. 2002, doi: 10.1109/TUFFC.2002.1009328.

[21] H. Torp, "Clutter rejection filters in color flow imaging: A theoretical approach," *IEEE Trans. Ultrason., Ferroelectr., Freq. Control*, vol. 44, no. 2, pp. 417–424, Mar. 1997, doi: 10.1109/58.585126.

[22] S. Bjaerum, H. Torp, and K. Kristoffersen, "Clutter filter design for ultrasound color flow imaging," *IEEE Trans. Ultrason., Ferroelectr., Freq. Control*, vol. 49, no. 2, pp. 204–216, Feb. 2002.

[23] J. Tierney, C. Coolbaugh, T. Towse, and B. Byram, "Adaptive clutter demodulation for non-contrast ultrasound perfusion imaging," *IEEE Trans. Med. Imag.*, vol. 36, no. 9, pp. 1979–1991, Sep. 2017, doi: 10.1109/TMI.2017.2714901.

[24] U.-W. Lok *et al.*, "Real time SVD-based clutter filtering using randomized singular value decomposition and spatial downsampling for micro-vessel imaging on a verasonics ultrasound system," *Ultrasonics*, vol. 107, Sep. 2020, Art. no. 106163, doi: 10.1016/j.ultras.2020.106163.

[25] C. Xu, J. H. Choi, K. Comess, and Y. Kim, "Color Doppler and spectral Doppler with high frame-rate imaging," in *Proc. IEEE Int. Ultrason. Symp.*, San Diego, CA, USA, Oct. 2010, pp. 1562–1566, doi: 10.1109/ULTSYM.2010.5935670.

[26] M. Kim, Y. Zhu, J. Hedhli, L. W. Dobrucki, and M. F. Insana, "Multidimensional clutter filter optimization for ultrasonic perfusion imaging," *IEEE Trans. Ultrason., Ferroelectr., Freq. Control*, vol. 65, no. 11, pp. 2020–2029, Nov. 2018, doi: 10.1109/TUFFC.2018.2868441.

[27] M. Kim, C. K. Abbey, J. Hedhli, L. W. Dobrucki, and M. F. Insana, "Expanding acquisition and clutter filter dimensions for improved perfusion sensitivity," *IEEE Trans. Ultrason., Ferroelectr., Freq. Control*, vol. 64, no. 10, pp. 1429–1438, Oct. 2017, doi: 10.1109/TUFFC.2017.2719942.

[28] M.-L. Li, "Adaptive imaging using principal-component-synthesized aperture data," in *Proc. IEEE Ultrason. Symp.*, Beijing, China, Nov. 2008, pp. 1076–1079, doi: 10.1109/ULTSYM.2008.0259.

[29] F. Vignon, J. S. Shin, S.-W. Huang, and J.-L. Robert, "Adaptive ultrasound clutter rejection through spatial eigenvector filtering," in *Proc. IEEE Int. Ultrason. Symp. (IUS)*, Washington, DC, USA, Sep. 2017, pp. 1–4, doi: 10.1109/ULTSYM.2017.8092061.

[30] L. D. Lathauwer, B. D. Moor, and J. Vandewalle, "A multilinear singular value decomposition," *SIAM J. Matrix Anal. Appl.*, vol. 21, no. 4, pp. 1253–1278, Jan. 2000, doi: 10.1137/S0895479896305696.

[31] T. G. Kolda and B. W. Bader, "Tensor decompositions and applications," *SIAM Rev.*, vol. 51, no. 3, pp. 455–500, Aug. 2009.

[32] R. R. Nadakuditi and A. Edelman, "Sample eigenvalue based detection of high-dimensional signals in white noise using relatively few samples," *IEEE Trans. Signal Process.*, vol. 56, no. 7, pp. 2625–2638, Jul. 2008, doi: 10.1109/TSP.2008.917356.

[33] M. A. Lediju, G. E. Trahey, B. C. Byram, and J. J. Dahl, "Short-lag spatial coherence of backscattered echoes: Imaging characteristics," *IEEE Trans. Ultrason., Ferroelectr., Freq. Control*, vol. 58, no. 7, pp. 1377–1388, Jul. 2011, doi: 10.1109/TUFFC.2011.1957.

[34] P.-C. Li and M.-L. Li, "Adaptive imaging using the generalized coherence factor," *IEEE Trans. Ultrason., Ferroelectr., Freq. Control*, vol. 50, no. 2, pp. 128–141, Feb. 2003, doi: 10.1109/TUFFC.2003.1182117.

[35] M. K. Jeong and S. J. Kwon, "Estimation of side lobes in ultrasound imaging systems," *Biomed. Eng. Lett.*, vol. 5, no. 3, pp. 229–239, Sep. 2015, doi: 10.1007/s13534-015-0194-y.

[36] J. Camacho, M. Parrilla, and C. Fritsch, "Phase coherence imaging," *IEEE Trans. Ultrason., Ferroelectr., Freq. Control*, vol. 56, no. 5, pp. 958–974, May 2009, doi: 10.1109/TUFFC.2009.1128.

[37] P. M. Shankar, "A compound scattering pdf for the ultrasonic echo envelope and its relationship to K and Nakagami distributions," *IEEE Trans. Ultrason., Ferroelectr., Freq. Control*, vol. 50, no. 3, pp. 339–343, Mar. 2003, doi: 10.1109/TUFFC.2003.1193628.

[38] P. Mohana Shankar, "A general statistical model for ultrasonic backscattering from tissues," *IEEE Trans. Ultrason., Ferroelectr., Freq. Control*, vol. 47, no. 3, pp. 727–736, May 2000, doi: 10.1109/58.842062.
[39] N. Wang, X. Song, and J. Cheng, "Generalized method of moments estimation of the Nakagami-m fading parameter," *IEEE Trans. Wireless Commun.*, vol. 11, no. 9, pp. 3316–3325, Sep. 2012, doi: 10.1109/TWC.2012.071612.111838.
[40] A. Abdi and M. Kaveh, "Performance comparison of three different estimators for the Nakagami m parameter using Monte Carlo simulation," *IEEE Commun. Lett.*, vol. 4, no. 4, pp. 119–121, Apr. 2000, doi: 10.1109/4234.841316.
[41] A. Rodriguez-Molares *et al.*, "The ultrasound toolbox," in *Proc. IEEE Int. Ultrason. Symp. (IUS)*, Washington, DC, USA, Sep. 2017, pp. 1–4, doi: 10.1109/ULTSYM.2017.8092389.
[42] N. Vervliet, O. Debals, L. Sorber, B. M. Van, and L. L. De. *Tensorlab | A MATLAB Package for Tensor Computations*. Accessed: Apr. 23, 2020. [Online]. Available: https://www.tensorlab.net/
[43] A. J. Y. Chee and A. C. H. Yu, "Receiver-operating characteristic analysis of eigen-based clutter filters for ultrasound color flow imaging," *IEEE Trans. Ultrason., Ferroelectr., Freq. Control*, vol. 65, no. 3, pp. 390–399, Mar. 2018, doi: 10.1109/TUFFC.2017.2784183.
[44] J. A. Jensen and N. B. Svendsen, "Calculation of pressure fields from arbitrarily shaped, apodized, and excited ultrasound transducers," *IEEE Trans. Ultrason., Ferroelectr., Freq. Control*, vol. 39, no. 2, pp. 262–267, Mar. 1992, doi: 10.1109/58.139123.
[45] J. A. Jensen, "FIELD: A program for simulating ultrasound systems," in *Proc. 10th Nordicbaltic Conf. Biomed. Imag.*, vol. 4, 1996, pp. 351–353.
[46] T. Loupas, J. T. Powers, and R. W. Gill, "An axial velocity estimator for ultrasound blood flow imaging, based on a full evaluation of the Doppler equation by means of a two-dimensional autocorrelation approach," *IEEE Trans. Ultrason., Ferroelectr., Freq. Control*, vol. 42, no. 4, pp. 672–688, Jul. 1995, doi: 10.1109/58.393110.
[47] S.-L. Wang, M.-L. Li, and P.-C. Li, "Estimating the blood velocity vector using aperture domain data," *IEEE Trans. Ultrason., Ferroelectr., Freq. Control*, vol. 54, no. 1, pp. 70–78, Jan. 2007, doi: 10.1109/TUFFC.2007.212.
[48] X. Mestre, "Improved estimation of eigenvalues and eigenvectors of covariance matrices using their sample estimates," *IEEE Trans. Inf. Theory*, vol. 54, no. 11, pp. 5113–5129, Nov. 2008, doi: 10.1109/TIT.2008.929938.
[49] J. J. Dahl *et al.*, "Coherence beamforming and its applications to the difficult-to-image patient," in *Proc. IEEE Int. Ultrason. Symp. (IUS)*, Sep. 2017, pp. 1–10, doi: 10.1109/ULTSYM.2017.8091607.
[50] K. Ozgun and B. Byram, "A general framework for channel domain SVD clutter filtering," in *Proc. IEEE Int. Ultrason. Symp. (IUS)*, Glasgow, U.K., Oct. 2019, pp. 2246–2248, doi: 10.1109/ULTSYM.2019.8925935.
[51] N. Vannieuwenhoven, R. Vandebril, and K. Meerbergen, "A new truncation strategy for the higher-order singular value decomposition," *SIAM J. Sci. Comput.*, vol. 34, no. 2, pp. A1027–A1052, Jan. 2012, doi: 10.1137/110836067.
[52] Y. Desailly, A.-M. Tissier, J.-M. Correas, F. Wintzenrieth, M. Tanter, and O. Couture, "Contrast enhanced ultrasound by real-time spatiotemporal filtering of ultrafast images," *Phys. Med. Biol.*, vol. 62, no. 1, pp. 31–42, Dec. 2016, doi: 10.1088/1361-6560/62/1/31.
[53] J. Brown *et al.*, "Investigation of microbubble detection methods for super-resolution imaging of microvasculature," *IEEE Trans. Ultrason., Ferroelectr., Freq. Control*, vol. 66, no. 4, pp. 676–691, Apr. 2019, doi: 10.1109/TUFFC.2019.2894755.
[54] S. Adabi, S. Ghavami, M. Fatemi, and A. Alizad, "Non-local based denoising framework for *in vivo* contrast-free ultrasound microvessel imaging," *Sensors*, vol. 19, no. 2, p. 245, Jan. 2019, doi: 10.3390/s19020245.
[55] O. M. H. Rindal, A. Rodriguez-Molares, and A. Austeng, "The dark region artifact in adaptive ultrasound beamforming," in *Proc. IEEE Int. Ultrason. Symp. (IUS)*, Washington, DC, USA, Sep. 2017, pp. 1–4, doi: 10.1109/ULTSYM.2017.8092255.
[56] S. Waraich, "Robust eigen-filter design for ultrasound flow imaging using a multivariate clustering," M.S. thesis, Univ. Waterloo, Waterloo, ON, Canada. [Online]. Available: http://hdl.handle.net/10012/15544

Kathryn A. Ozgun (Graduate Student Member, IEEE) was born in Chapel Hill, NC, USA, in 1994. She received the B.S. degree in biomedical engineering from North Carolina State University, Raleigh, NC, in 2016. She is currently pursuing the Ph.D. degree in biomedical engineering with Vanderbilt University, Nashville, TN, USA.

She is a Russel G. Hamilton Scholar with Vanderbilt University and holds a Graduate Certificate in surgical and interventional engineering. She is currently an Affiliate of the Vanderbilt Institute for Surgery and Engineering (VISE), Nashville, and the Vanderbilt University Institute of Imaging Science (VUIIS), Nashville. Her research is focused on coherence-based beamforming and adaptive filtering methods for ultrasound blood flow imaging.

Brett C. Byram (Member, IEEE) received the B.S.E. degree in biomedical engineering and mathematics from Vanderbilt University, Nashville, TN, USA, in 2004, and the Ph.D. degree in biomedical engineering from Duke University, Durham, NC, USA, in 2011.

He has spent time with the Siemens' Ultrasound Business Unit, Mountain View, CA, USA, and he spent a year working with the Jorgen Jensen's Center for Fast Ultrasound, Lyngby, Denmark. He served as an Assistant Research Professor with Duke University, from 2012 to 2013. He is part of the Vanderbilt Institute for Surgery and Engineering (VISE), Nashville, and is an Affiliate of the Vanderbilt University Institute of Imaging Science (VUIIS), Nashville. He is currently an Associate Professor with the Vanderbilt University School of Engineering, Nashville.